



1 **Simulating the Holocene deglaciation across a marine terminating portion of southwestern**
2 **Greenland in response to marine and atmospheric forcings**

3
4 Joshua K. Cuzzone¹, Nicolás E. Young², Mathieu Morlighem³, Jason P. Briner⁴, Nicole-Jeanne
5 Schlegel⁵

6
7 1University of California Los Angeles, Los Angeles, CA, USA
8 2Lamont-Doherty Earth Observatory, Columbia University, New York, NY, USA
9 3Department of Earth Sciences, Dartmouth College, Hanover, NH, USA.
10 4Department of Geology, University at Buffalo, Buffalo, NY, USA
11 5NASA Jet Propulsion Laboratory, California Institute of Technology, Pasadena, CA, USA.

12
13 *Correspondence to:* Joshua K. Cuzzone (Joshua.K.Cuzzone@jpl.nasa.gov)

14 **Abstract**

15
16 Numerical simulations of the Greenland Ice Sheet (GrIS) over geologic timescales can greatly
17 improve our knowledge of the critical factors driving GrIS demise during climatically warm
18 periods, which has clear relevance for better predicting GrIS behavior over the upcoming
19 centuries. To assess the fidelity of these modeling efforts, however, observational constraints of
20 past ice-sheet change are needed. Across southwestern Greenland, geologic records detail
21 Holocene ice retreat across both terrestrial-based and marine terminating environments, providing
22 an ideal opportunity to rigorously benchmark model simulations against geologic reconstructions
23 of ice-sheet change. Here, we present regional ice sheet modeling results using the Ice-sheet and
24 Sea-level System Model (ISSM) of Holocene ice sheet history across an extensive fjord region in
25 southwestern Greenland covering the landscape around the Kangiata Nunaata Sermia (KNS)
26 glacier and extending outward along the 200 km Godthåbsfjord. Our simulations, forced by novel
27 reconstructions of Holocene climate and recently implemented calving laws, assess the sensitivity
28 of ice retreat across the KNS region to atmospheric and oceanic forcing. Our simulations reveal
29 that the geologically reconstructed ice retreat across the bedrock landscape above sea-level in the
30 study area was likely driven by fluctuations in surface mass balance in response to early Holocene
31 warming – and likely not influenced significantly by the response of adjacent outlet glaciers to
32 calving and ocean-induced melting. The impact of ice calving within fjords, however, plays a
33 significant role by enhancing ice discharge at the terminus, leading to interior thinning up to the
34 ice divide that is consistent with reconstructed magnitudes of early Holocene ice thinning. Our
35 results, benchmarked against geologic constraints of past ice margin change, suggest that while
36 calving did not strongly influence Holocene ice margin migration across terrestrial portions of the
37 KNS forefield, it strongly impacted regional mass loss. While these results may provide an analog
38 to how similar fjord-dominated regions of the GrIS may respond to future warming, they also
39 illustrate that implementation and resolution of ice calving in paleo ice flow modeling is important
40 towards making more robust estimations of past ice mass change.

41
42 **1. Introduction**

43
44 Over the past few decades, the Greenland Ice Sheet (GrIS) has experienced accelerating ice mass
45 loss driven by increases in surface melt, runoff, and dynamic ice loss at marine terminating margins



46 (IMBIE, 2019). While projected mass loss from the GrIS is expected to be driven increasingly by
47 its surface mass balance (smb; Enderlin et al., 2014; Vizcaino et al., 2015; Goelzer et al., 2020)
48 and attendant meltwater runoff (Fettweis et al., 2008; Lenaerts et al., 2018), considerable
49 uncertainty exists regarding how oceanic forcing will influence GrIS mass loss, particularly
50 through ice calving processes (Goelzer et al., 2020; Choi et al., 2021). The satellite-based
51 observational record of GrIS change only spans a few decades making it difficult to identify and
52 disentangle the key drivers of GrIS mass change, and to understand over which timescales they
53 operate. Fortunately, geologic records detailing the retreat history of the GrIS provide an
54 important metric for evaluating numerical ice sheet models and help pinpoint the contributions of
55 various driving mechanisms to GrIS change. When combined, numerical ice sheet models and
56 geologic reconstructions can provide key insights into GrIS behavior in a warming climate across
57 centennial to millennial timescales.

58
59 The current interglaciation, the Holocene (the last 11.7 ka), is characterized by prolonged warmth
60 with proxy records suggesting that temperatures during the early to middle Holocene were 3 ± 1 °C
61 warmer than the pre-industrial period (Briner et al., 2016; Lecavalier et al., 2017), which drove
62 widespread retreat of the GrIS margin at a rate of ice mass loss exceeding 20th century values
63 (1900-2000 CE Young and Briner, 2015; Briner et al., 2020). Across Southwestern Greenland, a
64 detailed geologic record of Holocene ice-margin retreat encompassing both terrestrial and marine
65 terminating environments exists, providing an ideal testbed for ice sheet models to test the
66 sensitivity of past ice margin migration to atmospheric and marine forcings (Larsen et al., 2014;
67 Lesnek et al., 2020; Young et al., 2020; Young et al., 2021). Where land-based ice existed, well-
68 dated moraine sequences constrain ~120 km of ice retreat from the present-day coastline to just
69 outboard of the present-day ice margin (Lesnek et al., 2020; Young et al., 2020), and have been
70 shown by ice sheet models to be driven by negative smb in response to early Holocene warming
71 (Cuzzone et al., 2019; Downs et al., 2020; Briner et al., 2020).

72
73 Unlike the land-based portions of Southwest Greenland however, across the marine based region
74 covering the forefield around Kangiata Nunaata Sermia (KNS; Figure 1), it remains unknown what
75 drove this rapid ice margin retreat during the early Holocene (Young et al., 2021). While links
76 between atmospheric warming and runoff induced terminus retreat have been implicated as
77 reasons for the most recent historical retreat across the KNS region (Lea et al., 2014a,b), the longer
78 term triggers of rapid Holocene ice retreat are not constrained by the geologic data alone. Because
79 of the well dated chronology detailing Holocene ice retreat across this region however, ice sheet
80 models are well poised to address questions surrounding the scales of influence atmospheric and
81 oceanic forcings play on long term ice margin and mass change.

82
83 Building on recent advances in calving front dynamics in the Ice Sheet and Sea-level System
84 Model (ISSM; Larour et al., 2012), we use a high-resolution regional ice sheet model to investigate
85 the Holocene ice retreat across the KNS forefield. Our simulations build on prior ice modeling
86 efforts across Southwestern Greenland that were driven by novel reconstructions of past climate
87 (Badgeley et al., 2020; Briner et al., 2020). Where our past ice flow modeling efforts excluded ice
88 ocean-interactions (Briner et al., 2020), our simulations presented here take advantage of recent
89 implementation of physically based calving schemes in ISSM to specifically address how
90 Holocene ice retreat across the KNS forefield was influenced by marine and atmospheric forcing's.



91 Moreover, this work provides a foundation for future experiments using ISSM to simulate the
92 influence of ice-ocean interactions on the Holocene variability of the broader GrIS.
93

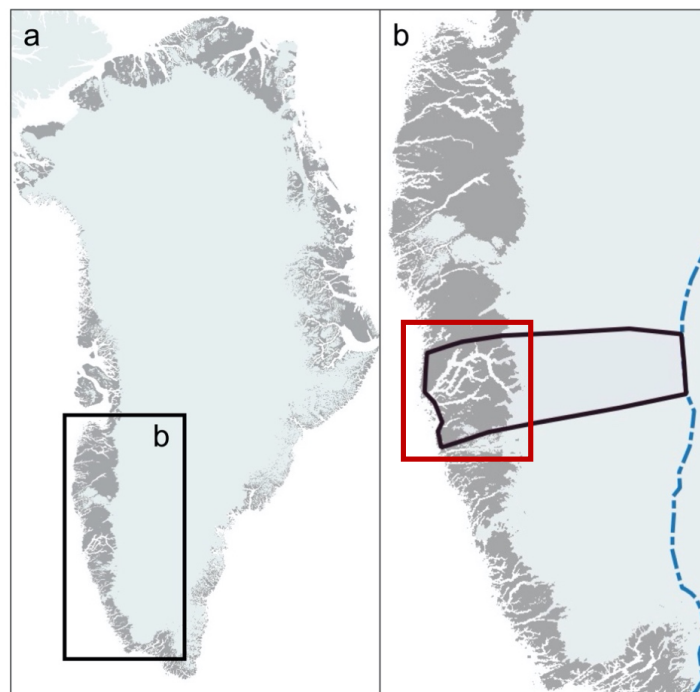


Figure 1. a.) The Greenland Ice Sheet. Highlighted is southwestern Greenland, where the ice model domain resides. b.) Southwestern Greenland. The ice model domain is outlined (bold black line), extending between the present-day coastline and ice divide (dashed blue line; Rignot and Mouginot, 2012). The red box corresponds to the area in figures 5, 6 and 8.

94

95 **2. Holocene Ice Retreat across the KNS Forefield**

96

97 Decades of radiocarbon dating and, more recently, cosmogenic ^{10}Be dating, track the retreat of the
98 GrIS in the KNS region through the Holocene (Weidick et al., 2012 and references therein; Larsen
99 et al., 2014; Young et al., 2021). Minimum-limiting radiocarbon ages from the outer coast near
100 Nuuk range from ca. 11.2 to 10.6 ka BP., which is mimicked by ^{10}Be ages of ca. 10.7 and 10.4 ka
101 BP (Figure 2). Between the outer coast and the modern GrIS margin at KNS are numerous
102 radiocarbon and ^{10}Be ages that are largely indistinguishable and require rapid deglaciation of the
103 region spanning about a millennium (Weidick et al., 2012; Larsen et al., 2014; Young et al., 2021).
104 Perhaps most relevant here are ^{10}Be ages in the immediate KNS region from just beyond the
105 historical ice limit that suggest KNS had retreated within or near its current position by ca. 10.3 ka
106 (Young et al., 2021). Radiocarbon ages from raised marine deposits, which require ice-free
107 conditions, adjacent to the main KNS fjord appear slightly younger than regional ^{10}Be ages. These
108 radiocarbon ages, however, are minimum-limiting ages and an upfjord radiocarbon age of ca. 10.2
109 ka from a bivalve reworked by a KNS readvance requires that the main fjord deglaciated prior to
110 ca. 10.2 ka (Figure 2). Collectively, the radiocarbon and ^{10}Be ages suggest rapid and synchronous



111 deglaciation of both the landscape and fjord systems between the outer coast near Nuuk and the
112 modern margin at KNS. Lastly, ^{10}Be ages from slightly beyond the historical limit to the north and
113 south of KNS are slightly younger suggesting that these ice margins may have lagged behind ice
114 retreat in the immediate KNS region (Figure 2).
115

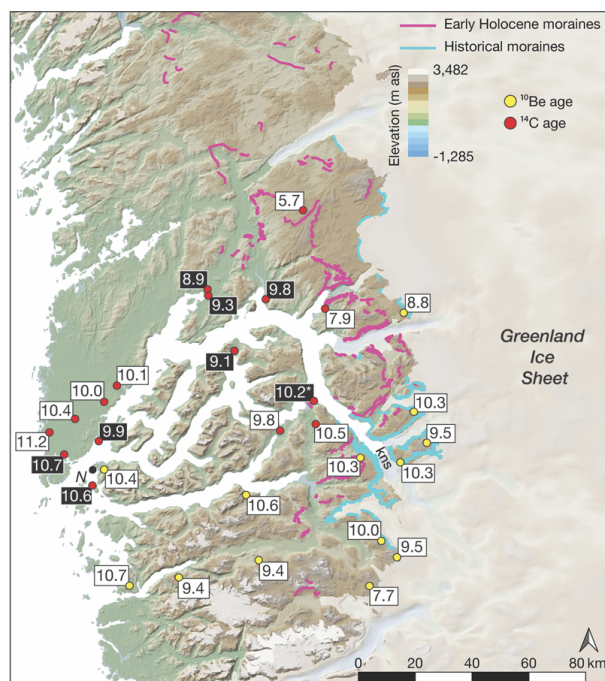


Figure 2. KNS region with geological constraints that track GrIS retreat in the early Holocene. Radiocarbon ages (red circles) and ^{10}Be ages (yellow circles) are from Weidick et al. (2012), Larsen et al. (2014), and Young et al. (2021). For figure clarity, we only show the mean deglaciation age at each site (see Young et al., 2021 for full site descriptions). Radiocarbon and ^{10}Be across the immediate KNS region are similar and reveal that deglaciation of the coast occurred ca. 11.2-10.7 ka and KNS had retreated near or within its modern extent by ca. 10.3 ka. Radiocarbon ages in white text and black background are from marine deposits and constrain the timing of retreat within the main fjord. Figure has been modified from Young et al. (2021).

116
117
118
119
120

3. Model description and setup

3.1 Ice Sheet Model

121
122
123
124
125
126

We rely on ISSM, a thermomechanical finite-element ice sheet model, to simulate the Holocene ice history across the KNS forefield, and follow similar published model setups (Cuzzone et al, 2019; Briner et al., 2020). The higher-order approximation of Blatter (1995) and Pattyn (2003) is used to solve the momentum balance equations. Our model domain centers on the KNS and Godthåbsfjord forefield, extending from the present-day coastline, where geologic observations show ice resided at the end of the Younger Dryas (Larsen et al., 2014; Lesnek et al., 2020) to the



127 present-day ice divide (Figure 1b; Rignot and Mouginot, 2012). The northern and southern
128 boundaries of our model domain are chosen to represent regions of minimal north-south across
129 boundary flow based on Holocene ice sheet simulations of southwestern Greenland (Briner et al.,
130 2020). Anisotropic mesh adaptation is used to create a non-uniform model mesh that varies based
131 upon gradients in bedrock topography from BedMachine v3 (Morlighem et al., 2017). Because
132 fjord width across our domain is often <5 km and high-resolution grids are necessary for capturing
133 grounding line dynamics (1 km; Seroussi and Morlighem, 2018), the horizontal mesh resolution
134 varies from 1 km in fjords and areas of high bedrock relief to 15 km where the bedrock relief is
135 low (Figure 3).

136

137 To capture the thermal evolution of the ice, our model uses an enthalpy formulation (Aschwenden
138 et al., 2012) that captures both temperate and cold ice. We impose transient air temperatures at
139 the surface and a constant but spatially varying geothermal heat flux at the base (Shapiro and
140 Ritzwoller, 2004) and our model contains only five vertical layers in order to reduce computational
141 load (Cuzzone et al., 2018; Cuzzone et al., 2019). In order to capture sharp thermal gradients near
142 the base and simulate the vertical distribution of temperature within the ice, we use quadratic finite
143 elements (P1xP2) along the z-axis for the vertical interpolation following Cuzzone et al. (2018).
144 This methodology has been successfully applied to simulate the transient behavior of the GrIS
145 across geologic timescales and the contemporary period (Cuzzone et al., 2019; Briner et al., 2020;
146 Smith-Johnson et al., 2020).

147

148 We use a linear friction law and, similar to Briner et al. (2020), we construct a spatially varying
149 basal friction coefficient (k) under areas covered by the present-day ice sheet using inverse
150 methods (Morlighem et al., 2010; Larour et al., 2012) that satisfies the best match between
151 modeled and satellite-derived surface velocities (Rignot and Mouginot, 2012):

152

$$153 \quad \tau_b = -k^2 N v_b \quad (1)$$

154

155 where τ_b represents the basal stress, N represents the effective pressure, and v_b is the magnitude
156 of the basal velocity. For contemporary ice-free areas, a spatially varying basal friction coefficient
157 is constructed to be proportional to bedrock elevation following Åkesson et al., 2018:

158

$$159 \quad k = 100 \times \frac{\min[\max(0, z_b + 800), z_b]}{\max(z_b)} \quad (2)$$

160

161 where z_b is the height of the bedrock with respect to sea level. For these parametrizations, the
162 friction coefficient is low within fjords and is larger over areas of high topographic relief. This
163 basal friction coefficient is allowed to vary through time based upon changes in the simulated basal
164 temperature following Cuzzone et al. (2019). As simulated basal ice temperatures decrease with
165 respect to present day, the friction coefficient will increase, and therefore sliding will decrease.
166 The opposite occurs when simulated basal temperatures are warm relative to present day. Lastly,
167 the ice rheology parameter B is temperature-dependent, following rate factors in Cuffey and
168 Paterson (2010), and is initialized by solving for a present day thermal steady state and allowed to
169 vary during transient simulations (Cuzzone et al., 2018; 2019).

170

171



172
173
174
175

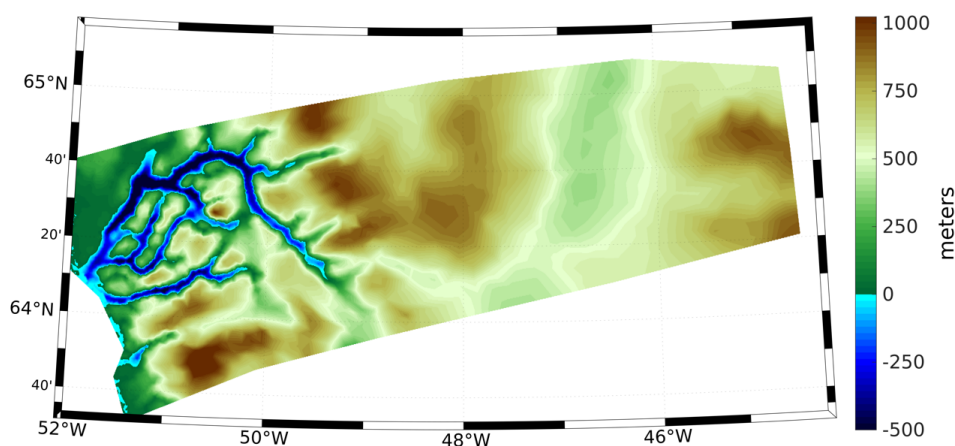


Figure 3. Bedrock topography for the model domain. Blue colors indicate areas that are below present-day sea level.

176

177 **3.2 Ice Front Migration and Calving**

178

179 We use the level-set method to track the motion of the ice front (Bondzio et al., 2016). The velocity
180 of the moving ice front is calculated as:

181

$$182 \quad v_f = v - (c + \dot{M}) n \quad (3)$$

183

184 where v_f is the ice velocity vector, v is the ice velocity vector at the ice front, c is the calving rate,
185 \dot{M} is the melting rate of the calving front, and n is the unit normal vector pointing horizontally
186 outward from the calving front. For these simulations, we assume that the melting rate at the
187 calving front is negligible compared to the calving rate.

188

189 To simulate calving, we rely on the physically-based Von Mises stress calving (Morlighem et al.,
190 2016), whereby the calving rate is related to tensile stresses within the ice:

191

$$192 \quad c = \|v\| \frac{\tilde{\sigma}}{\sigma_{max}} \quad (4)$$

193

194 where $\tilde{\sigma}$ is the von Mises tensile strength, $\|v\|$ is the magnitude of the horizontal ice velocity, and
195 σ_{max} is the maximum stress threshold, which has separate values for grounded and floating ice.
196 Under this formulation, the ice front will remain stable when $\tilde{\sigma} = \sigma_{max}$, will retreat when $\tilde{\sigma} >$
197 σ_{max} , and will advance when $\tilde{\sigma} < \sigma_{max}$. Tensile strength measurements of ice show a range of
198 possible σ_{max} , ranging between 150 kPa to 3100 kPa (Petrovic 2003). For this study we choose



199 $\sigma_{max} = 600$ kPa for grounded ice and 200 kPa for floating ice, which is within the ranges used by
200 recent studies across Greenland (Bondzio et al., 2016; Morlighem et al., 2016; Choi et al., 2020).
201

202 3.3 Climate and Surface Mass Balance Reconstruction

203
204 We rely on a novel gridded paleoclimate reanalysis product that reconstructs the necessary climate
205 variables of temperature and precipitation needed to calculate the surface mass balance history
206 through the Holocene (Badgeley et al., 2020). Temperature was derived from oxygen-isotope
207 records from eight ice cores, and five ice core accumulation records were used to reconstruct
208 precipitation. This reanalysis relies on a data assimilation framework that combines the
209 information from ice core proxies with climate-model simulations of the last deglaciation (Liu et
210 al., 2009; He et al., 2013) to create a spatially complete (e.g., GrIS wide) and temporally consistent
211 reconstruction of past temperature and precipitation. This reconstruction agrees well with
212 independent proxies and previously published paleoclimate reconstructions (Badgeley et al.
213 (2020)). For new simulations presented here, we chose two end members of reconstructed
214 precipitation and temperature from Badgeley et al. (2020). The high temperature reconstruction
215 was chosen, which has a greater magnitude of early Holocene warming, and the low temperature
216 scenario, which has a more muted early Holocene warming (Figure 4a). Additionally, we choose
217 the high and low precipitation scenarios (Figure 4b), which differ in the magnitude and timing of
218 peak Holocene precipitation. These reconstructions span a plausible range of temperature and
219 precipitation scenarios as discussed in Badgeley et al. (2020).
220

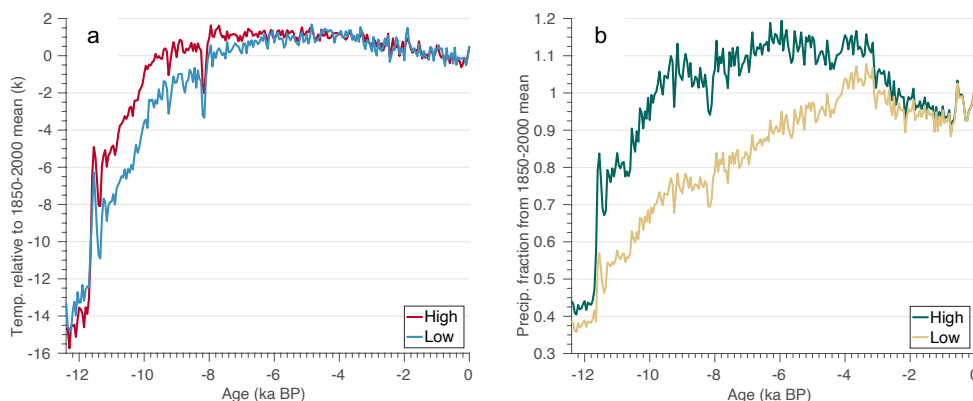


Figure 4. a) Area-averaged (over model domain) mean annual temperature anomaly (k) relative to the 1850-2000 mean for the High and Low temperature reconstructions from Badgeley et al. (2020). b) Area-averaged (over model domain) mean annual precipitation as a fraction from the 1850-2000 mean for the High and Low reconstructions from Badgeley et al. (2020).

221 The simulations discussed below use a combination of these forcings to address the possible role
222 of varying climatic conditions. Following prior work (Cuzzone et al., 2019; Briner et al., 2020),
223 we compute the surface mass balance over the Holocene using a positive degree day (PDD) method
224 (Tarasov and Peltier, 1999; Le Morzadec et al., 2015). For this scheme, snow melts first at 4.3
225 mm °C⁻¹day⁻¹, and the remaining positive degree days are used to melt bare ice at 8.3 °C⁻¹day⁻¹. A



226 lapse rate of 6 °C/km is used to adjust the temperature of the climate forcings to ice-surface
227 elevation, while an allowance for the formation of superimposed ice is permitted following
228 Janssens and Huybrechts (2000).

229

230 3.4 Experimental Setup

231

232 For the reanalysis discussed in section 3.3, temperature is expressed as anomalies from the AD
233 1850-2000 mean, and precipitation is expressed as a fraction of the AD 1850-2000 mean (Figure
234 4). Following Briner et al. (2020), we apply these anomalies onto the 1850-2000 monthly mean
235 climatology of temperature and precipitation from Box et al. (2013) to produce the necessary
236 Holocene temperature and precipitation forcings:

237

$$238 T_t = \bar{T}_{(1850-2000)} + \Delta T_t \quad (5)$$

239

$$240 P_t = \bar{P}_{(1850-2000)} \times \Delta P_t \quad (6)$$

241

242 where $\bar{T}_{(1850-2000)}$ and $\bar{P}_{(1850-2000)}$ are the monthly mean temperature and precipitation over AD
243 1850-2000 from Box et al. (2013) and ΔT_t and ΔP_t are the monthly anomalies from Badgeley et al.
244 (2020). We perform four transient model simulations using four combinations of possible climate
245 scenarios shown in Table 1. For each climate scenario, we run two simulations. First, simulations
246 are performed where the calving parameterization is turned on (denoted as ‘Calving On’). Second,
247 simulations are performed where the calving parameterization is turned off (denoted as ‘Calving
248 Off’). For these simulations, we apply a temporally constant melting rate under floating ice of 40
249 m/yr. We also perform additional simulations discussed further in section 4.4 to assess sensitivity
250 to the calving maximum stress thresholds and ocean-induced melt-rates.

251

252 We initialize our regional ice-sheet model using present-day ice-surface elevation from the
253 Greenland Ice Mapping Project digital elevation model (Howat et al., 2014). A constant climate
254 from 12,400 years ago is then applied for each experiment, allowing our model to reach
255 equilibrium in ice volume and basal temperature, which takes 20,000 years. Since our simulations
256 are regional in scale, we use boundary conditions of temperature, ice velocity, and thickness from
257 a recent ice sheet simulation of West-Southwest Greenland (Briner et al., 2020) and impose these
258 as Dirichlet boundary conditions at the southern, northern, and ice-divide boundaries. These
259 boundary conditions are forced transiently throughout the Holocene simulations and use similar
260 model setups and climate forcings as discussed here. Each model is then run transiently through
261 time from 12,400 years ago to AD 1850 using the climatologies discussed above, and then from
262 1850 to 2013 we use monthly temperature and precipitation fields from Box et al. (2013). We use
263 an adaptive timestep, which varies between 0.02 and 0.1 years, depending on the Courant–
264 Friedrichs–Lewy criterion (Courant et al., 1928).

265



266
267
268
269
270
271
272
273
274
275
276
277
278
279
280
281
282
283
284
285
286
287
288
289
290
291
292
293
294
295
296
297
298
299
300
301
302
303
304
305
306
307
308
309
310
311
312

	Temperature Scenario	Precipitation Scenario	Calving Parameterization
Experiment I	High	High	On
			Off
Experiment II	High	Low	On
			Off
Experiment III	Low	High	On
			Off
Experiment IV	Low	Low	On
			Off

Table 1. Description of model experiments. See Figure 4 for a display of the temperature and precipitation forcings scenarios.

4. Results

We spin up each model as described above (section 3.4) without the ice calving parametrization turned on. Only when we begin the transient simulation through the Holocene do we turn on the ice calving parametrization for the ‘Calving On’ scenarios (Table 1). Our transient simulations begin 12,400 years ago with the ice margin residing along the present-day coastline for all experiments, which is approximately consistent with where geologic constraints place the ice margin at that time (Young et al, 2021 and references therein).

4.1 Simulated Deglaciation

First, we assess how our simulated deglaciation compares with geologic reconstructions of ice sheet change in the KNS region. Geological constraints outlined above reveal that ice retreated across the KNS forefield rapidly in the early Holocene. While relatively little direct information exists detailing ice retreat within the fjords, the terrestrial portion of our domain (i.e., the inter-fjord bedrock landscape) became ice-free between ~11.2 ka and 9.5 ka as ice retreated from the modern coastline towards, and eventually surpassing, what is now the modern ice margin.

To compare against the geologic constraints, we determine when in time portions of our model domain become ice free (Figure 5). Since ice can readvance over areas that had been deglaciated during our simulations, we take the youngest age from which locations in our simulations became ice free. Our simulations illustrate clear differences in the timing of deglaciation across terrestrial surfaces above sea-level and within the fjords. For the high and low temperature scenarios, terrestrial surfaces deglacierate up to a few millennia earlier than the adjacent fjords. This difference in timing between the fjords and terrestrial surfaces is perhaps unsurprising given how fjord systems act as conduits draining the ice interior. This persistence of ice extent within the fjords despite elevated warming experienced during early to middle Holocene illustrates the role of ice dynamics, which is explored further in section 4.3.

For the high and low temperature scenarios, there is little difference between the age of deglaciation on terrestrial surfaces for simulations that allow (Figures 5a and 5b; Figures 6a and 6b) and do not allow calving (Figures 5d and 5e; Figures 6d and 6e). In contrast, deglaciation of terrestrial surfaces occurs later in Holocene for the simulations using the high precipitation



313 scenario than for those simulations using the low precipitation scenario. For simulations using the
314 high temperature scenario, these differences are up to 500 years (Figure 5). For the low temperature
315 scenarios, terrestrial surfaces deglciate up to 1000 years later for simulations using the high
316 precipitation forcing (Figure 6).

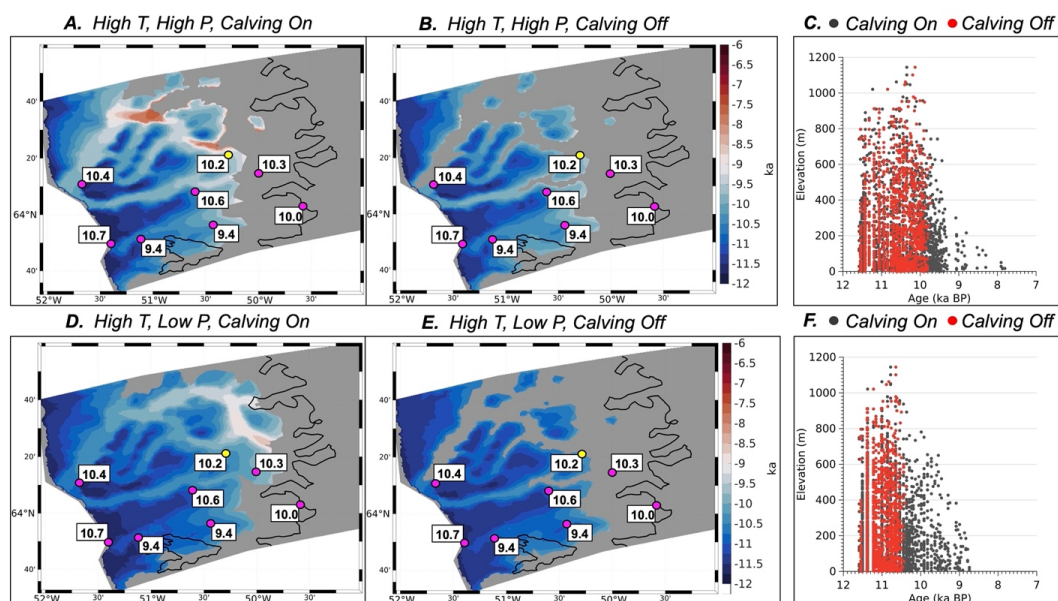


Figure 5. Map of simulated deglaciation ages for High temperature scenarios with A.) High precipitation, Calving On. B.) High precipitation, Calving Off. D.) Low precipitation, Calving On, and E.) Low precipitation – Calving off. Gray mask is the simulated ice extent at present day and the black line denotes the actual present day ice extent (Rignot and Mouginot, 2012). Magenta circles are the best estimate of the timing of deglaciation at that point based on ^{10}Be surface exposure ages in thousands of years ago and the yellow dot shows minimum limiting radiocarbon age (Young et al., 2021). Scatter plot of simulated deglaciation age (above sea level) versus bedrock elevation for C) High temperature, high precipitation, and F) High temperature, low precipitation. Red dots are from simulations without calving and black dots are for simulations with calving.

317
318 The larger sensitivity to the precipitation reconstruction on the timing of deglaciation for the lower
319 temperature scenario versus the high temperature scenario is similar to the results of Briner et al.
320 (2020). Across deglaciaded regions where the surface mass balance dictates ice margin migration,
321 increased precipitation modulates the temperature driven retreat in the early Holocene, particularly
322 for simulations with colder climates (Briner et al., 2020; Downs et al., 2020). As discussed above,
323 since calving does not appear to significantly influence terrestrial ice retreat across this region,
324 SMB may be the primary driver of ice retreat across terrestrial surfaces within our model domain
325 from which the majority of geologic constraints on past ice retreat are present. It is important to
326 note that, while calving does not seem to play a significant role in the retreat of ice across terrestrial



327 surfaces, simulations that allow calving have a more reduced ice extent (gray mask) at the end of
328 each simulation, which may indicate that calving limits ice front readvance within the fjord.

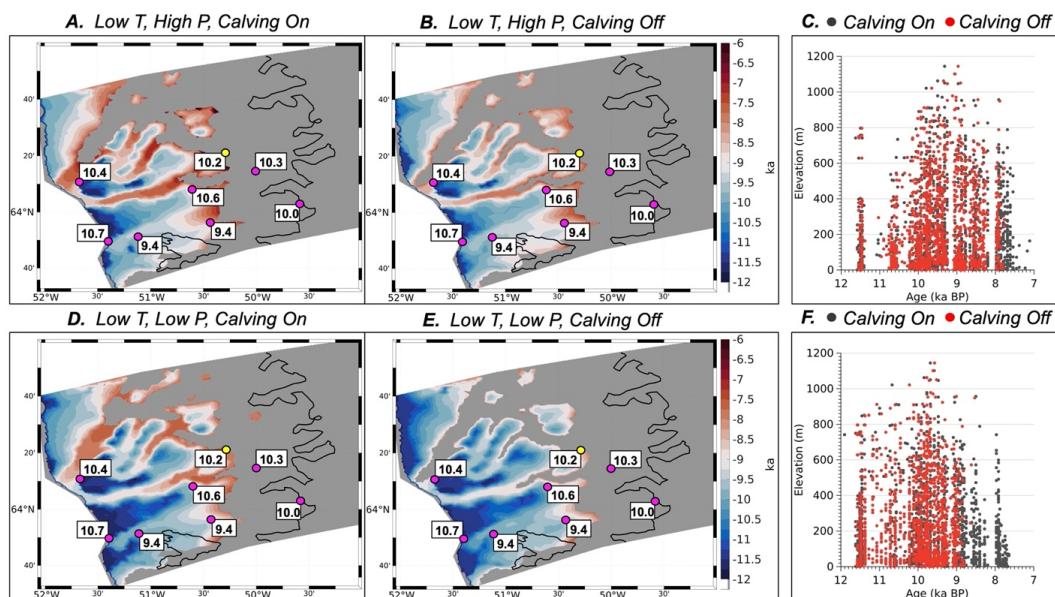


Figure 6. Map of simulated deglaciation ages for Low temperature scenarios with A.) High precipitation, Calving On. B.) High precipitation, Calving Off. D.) Low precipitation, Calving On, and E.) Low precipitation – Calving off. Gray mask is the simulated ice extent at present day and the black line denotes the actual present day ice extent (Rignot and Mouginot, 2012). Magenta circles are the best estimate of the timing of deglaciation at that point based on ^{10}Be surface exposure ages in thousands of years ago and the yellow dot shows a minimum limiting radiocarbon age that requires ice free conditions in the fjord at that time (Weidick et al., 2012; Young et al., 2021). Scatter plot of simulated deglaciation age (above sea level) versus bedrock elevation for C) Low temperature, high precipitation, and F) Low temperature, low precipitation. Red dots are from simulations without calving and black dots are for simulations with calving.

329
330 The manner in which deglaciation occurs on terrestrial surfaces can be an important factor in
331 determining the pace and magnitude of the ice margin response to warming. Geologic archives
332 constraining ice retreat across the KNS forefield span an elevational range of 1300 m, yet, no
333 elevational dependence on the age of deglaciation is evident (Larsen et al., 2014; Young et al.,
334 2021). This could indicate large scale ice margin retreat in response to rapid ice surface lowering,
335 but certainly precludes scenarios where ice surface lowering occurred slowly exposing high
336 elevation sites well before low elevation sites. To compare our simulated deglaciation history as
337 a function of elevation against the geologic data, we plot the simulated age of deglaciation against
338 elevation, and restrict our datapoints to terrestrial surfaces above sea level (Figure 5c and 5f; Figure
339 6c and 6f). In general, our simulations agree with the geologic data indicating that there was no
340 elevational dependence on the age of deglaciation; if there were any indication of an elevation
341 dependence on the age of deglaciation, we would observe that high elevation sites would become
342 ice free first, followed by low elevation sites. Instead, all of the plots show that deglaciation
343 happens simultaneously at discrete time intervals across all elevation bands, indicating that ice



344 surface lowering was rapid and coincident with ice margin pullback. These elevation-time
345 diagrams also highlight how the higher precipitation scenarios have later mean deglaciation ages
346 across terrestrial surfaces (Figure 5c and 6c) than corresponding simulations using the low
347 precipitation scenario (Figure 5f and 6f). We also note that for simulations where calving is turned
348 off (red dots), ice retreat appears to stop earlier than for those simulations with calving turned on
349 (black dots). This occurs because the simulations without calving experience a larger late
350 Holocene ice readvance than those simulations where calving is turned on (black dots). As a
351 consequence of this, model grid points that would have otherwise deglaciated prior to the
352 readvance are overrun with ice and therefore are not marked as deglaciated in the simulation.
353

354 Lastly, each of our experiments end with a simulated present-day ice extent that is beyond
355 (westward of) the actual present-day ice extent (Figure 5 and 6). Yet, the simulated ice-margin
356 position in the fjords is less extensive for all experiments where calving is permitted. Those
357 experiments that allow calving and used the high temperature scenario (Figure 5a and 5d) simulate
358 a present-day ice extent that is closer to the observed present-day margin when compared to
359 simulations using the low temperature forcing (Figure 6a and 6d).
360

361 **4.2 Ice mass evolution and minimum ice extent**

362

363 Broadly, scenarios that allow calving undergo greater ice mass loss than those simulations where
364 calving is not allowed (Figure 7; black lines). The differences in simulated ice mass also vary
365 depending on the climate scenarios used. For example, during early Holocene warming (12 ka -
366 8 ka), simulations that allow calving and use the high temperature scenarios (Figure 7a, b)
367 experience ice mass loss, while simulations that do not allow calving experience a period of ice
368 mass stability (Figure 7a, b; dashed red line), which is more prolonged in the simulation using the
369 high precipitation scenario (Figure 7a).
370

371 For the simulations using the low temperature scenario (Figure 7c, d), initial ice mass loss is
372 interrupted by brief increases in ice mass during the early Holocene (between 11 ka-10 ka). This
373 increase in ice mass occurs for both scenarios with and without calving (Figure 7c, d; black and
374 dashed red line), although the simulations without calving experience larger increases in ice mass
375 during this period. Accordingly, the low temperature simulation with higher precipitation (Figure
376 7c) experiences larger ice mass gain than the simulation using the low precipitation scenario
377 (Figure 7d). During this interval, precipitation is approximately 20-30% more for the high
378 precipitation scenario during the early Holocene than the low precipitation scenario. Much of this
379 mass gain is due to ice thickening over the interior of the model domain, where despite early
380 Holocene warming, colder temperatures (at higher elevations on the ice sheet) support snowfall
381 (see section 4.3).
382

383 Throughout the remainder of the Holocene, the evolution of ice mass for experiments using the
384 high temperature scenario (Figure 7a, b) differ from those simulations using the low temperature
385 scenario (Figure 7c, d). Simulations using the high temperature scenario (Figure 7a, b) reach a
386 minimum ice volume between 7.6-7.2 ka. For the simulation using the high precipitation scenario,
387 ice mass increases slightly following this minimum, and remains generally stable throughout the
388 remainder of the Holocene (Figure 7a), whereas the simulation using the low precipitation scenario
389 experiences large ice mass gain following this minimum, with steady growth occurring throughout

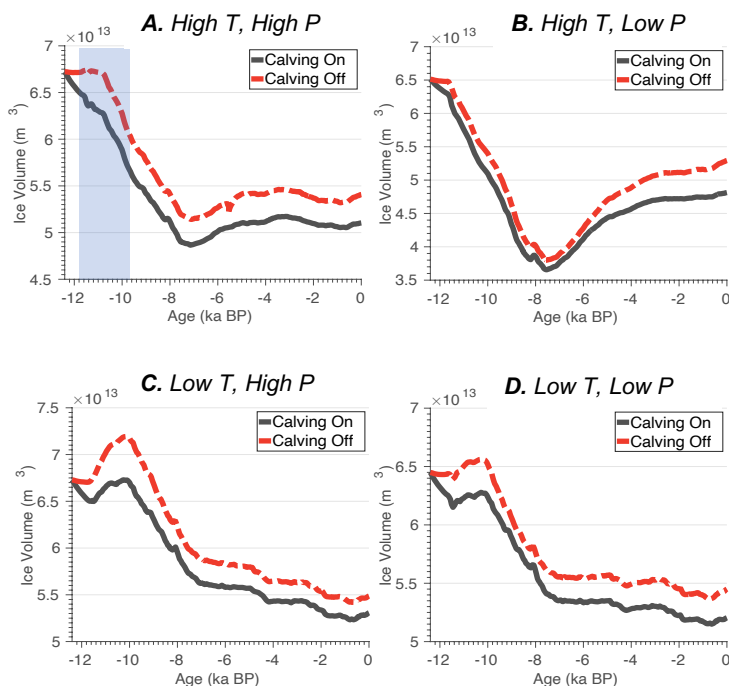


Figure 7. Holocene ice volume ($\times 10^{13} \text{ m}^3$) evolution for each model experiment. Refer to Table 1 for a summary of the climate forcings used in each experiment. Black lines denote those simulations with the calving parametrization turned on. Dashed red lines denote those simulations with the calving parametrization turned off. The vertical blue bar above marks a time period (12 ka – 10 ka) used for analysis presented in Figure 8 and 9.

390 the remainder of the simulation (Figure 7b). It is important to note, however, that for the high
391 temperature scenarios, this ice mass gain is more muted for simulations that allow calving. In
392 contrast, the simulations using the low temperature scenario (Figure 7c, d) lose the majority of ice
393 mass by 8–7 ka, with ice mass loss either continuing through the Holocene (Figure 7c) or remaining
394 relatively stable before reaching a minimum at 0.6–0.4 ka (Figure 7d).
395

396 Regional relative sea-level records reveal that sea level fell below modern between 4–3 ka, before
397 rising towards modern values (Long et al., 2011), interpreted to represent the re-loading of the
398 Earth’s crust as the GrIS readvanced during the late Holocene following a mid-Holocene
399 minimum. In addition, radiocarbon-dated lake sediments from southwestern Greenland suggest
400 that this sector of the GrIS likely achieved its minimum extent after ca. 5 ka, and that eastwards
401 retreat of the ice margin was likely minimal (Larsen et al., 2015; Young and Briner, 2015; Lesnek
402 et al., 2020; Young et al., 2021). Although no direct geological constraints on the minimum GrIS
403 ice extent during the Holocene exist, available constraints suggest that the large-scale ice margin
404 retreat inboard of the present-day extent as simulated by some ice sheet models in this sector (20–
405 40 km; Tarasov and Peltier, 2002; Lecavalier et al., 2014) is likely too extreme. Relying on these



406 geologic constraints, we can crudely assess the temporal and spatial patterns of the simulated ice
407 mass and minimum extent.
408
409 None of our simulations accurately capture the exact timing of the GrIS minimum in the KNS
410 region, but some simulations are likely better representations than others. Simulations using the
411 high temperature scenario (Figure 7a, b) achieve an ice mass minimum prior to 5 ka followed by
412 ice regrowth. The high temperature-low precipitation scenario depicts an extreme GrIS minimum
413 followed by significant regrowth. While of the overall pattern of a GrIS minimum followed by

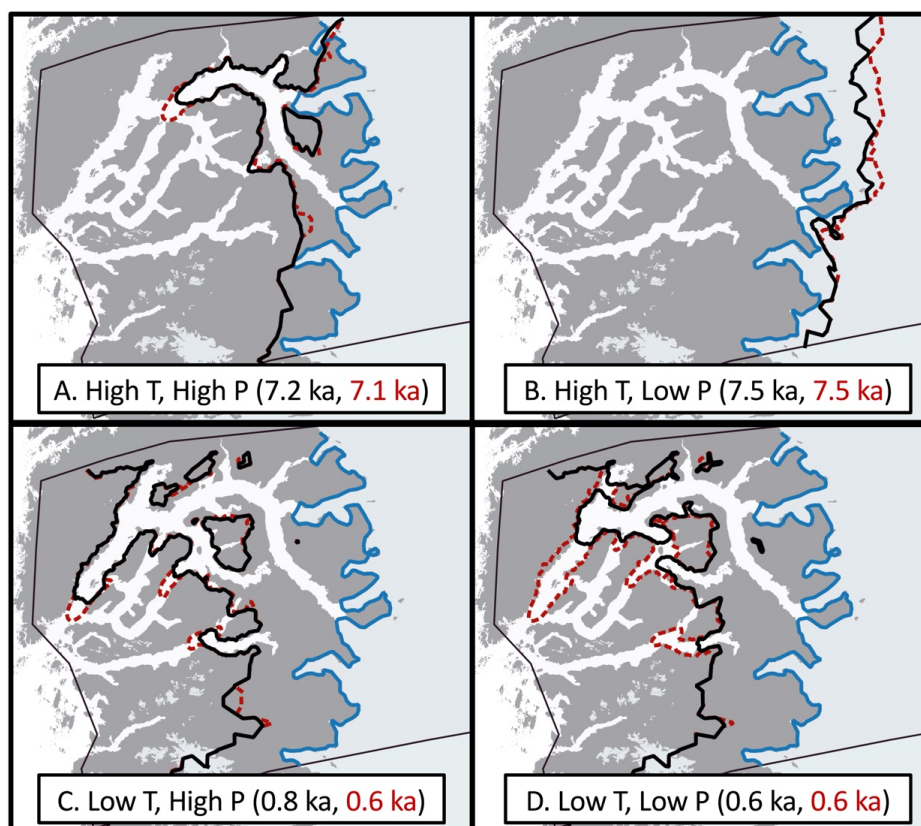


Figure 8. Age of minimum ice extent for each simulation (black text: simulations with calving, red text: simulations without calving). The black line denotes the minimum ice extent for simulations with calving. The dashed red line denotes the minimum ice extent for simulations without calving. The present-day ice extent is shown as the blue line.

414 regrowth is consistent with the geologic record, the magnitude of simulated change is likely
415 inconsistent with geological records, pointing to a rather modest GrIS minimum; although we do
416 acknowledge that minimal ice retreat as constrained by the geologic record does not necessarily
417 equate to muted mass loss. In contrast, the high temperature-high precipitation experiment depicts
418 an ice-mass minimum that is likely too early, but the magnitude of this minimum is less (Figure
419 7A). Moreover, ice regrowth following this minimum is restricted with only modest change



420 occurring over the last 6 kyr (Figure 7A). Although this simulated minimum is likely too early, a
421 simulated ice mass that undergoes minimal change over the last ~6 kyr is broadly consistent with
422 the geological record that depicts a minimum closer to ca. 4-3 ka, but where the GrIS margin likely
423 did not undergo significant change between ca. 7-3 ka (Young et al., 2021). Both low temperature
424 scenarios are inconsistent with the geological record as both show continued ice mass loss through
425 the Holocene. Although it is possible, but unlikely, that continued ice loss through the Holocene
426 could still be achieved if the ice margin retreated inland followed by a readvance toward its present
427 position, mass loss through the Holocene is inconsistent with relative sea-level records.

428
429 The minimum ice margin extent achieved in our simulations is shown in Figure 8. For the high
430 temperature scenarios (Figure 8a, b), the simulated minimum ice extent is either just outboard of
431 the present-day ice margin (Figure 8a; high precipitation) or inboard of the present-day ice margin
432 (Figure 8b; low precipitation). Because the geologic evidence supports that the Holocene ice
433 extent minimum was close to and perhaps slightly inboard of the present-day ice margin (Young
434 et al., 2021), both simulations are broadly consistent with the geological record. But, again, the
435 high temperature – high precipitation scenario depicts significant ice regrowth resulting in a
436 present-day ice margin significantly more extended than modern (Figure 5).

437 438 **4.3 Early Holocene Thinning** 439

440 Figures 9 and 10 show the simulated ice elevation changes for the time period between 12 ka to
441 10 ka for each experiment (highlighted in Figure 7a as the light blue vertical bar). During this time
442 period, widespread early Holocene warming drove increased ice melt along the margin of the
443 model domain. This pervasive thinning along the margin is captured in all model experiments
444 (Figure 9 and 10), although the amplitude of ice thinning is greatest for the experiments using the
445 high temperature scenario (Figure 9). Across all experiments, inland thickening occurs, however,
446 the magnitude of interior thickening is not solely influenced by the SMB, but is also influenced by
447 calving. For our experiments that allow calving, interior thickening is reduced and ultimately
448 influences the trend and magnitude of changes in simulated ice volume; simulations that allow
449 calving either experience increased ice mass loss (Figure 7a, b) or more muted ice mass gain
450 between 12 ka and 10 ka (Figure 7c, d). Additionally, the spatial pattern of elevation changes
451 shows that marginal thinning propagates farther upstream and into the ice sheet interior for
452 simulations that allow ice calving. This relationship continues throughout the remainder of the
453 Holocene, as experiments with calving either result in more mass loss than simulations without
454 calving, or more muted ice mass gain (see Figure 7). These variations in simulated Holocene ice
455 mass and ice surface elevation change can be linked to the influence ice calving has on ice front
456 position and stability, and ultimately the rate at which ice can flux through the fjord system. During
457 the time period of 12 ka to 10 ka, ice velocity differences for simulations with and without calving
458 are in excess of 200 m/yr along many fjords within the KNS region (Figure 11). Calving at the
459 ice front leads to increases in ice velocity within outlets across the model domain, thereby
460 promoting increased mass flux and transport from the ice interior to the margin. Thus, even though
461 the large-scale ice margin migration across our model domain is relatively insensitive to calving,
462 the overall mass budget and surface profile of the ice is strongly influenced by calving.

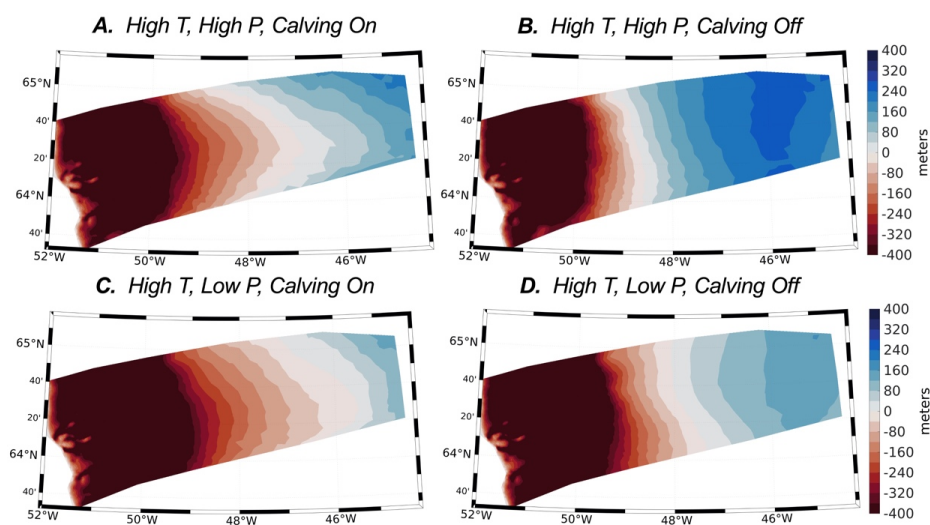


Figure 9. Simulated elevation changes (in meters) during period 12ka – 10ka shown for experiments using the high temperature forcing.

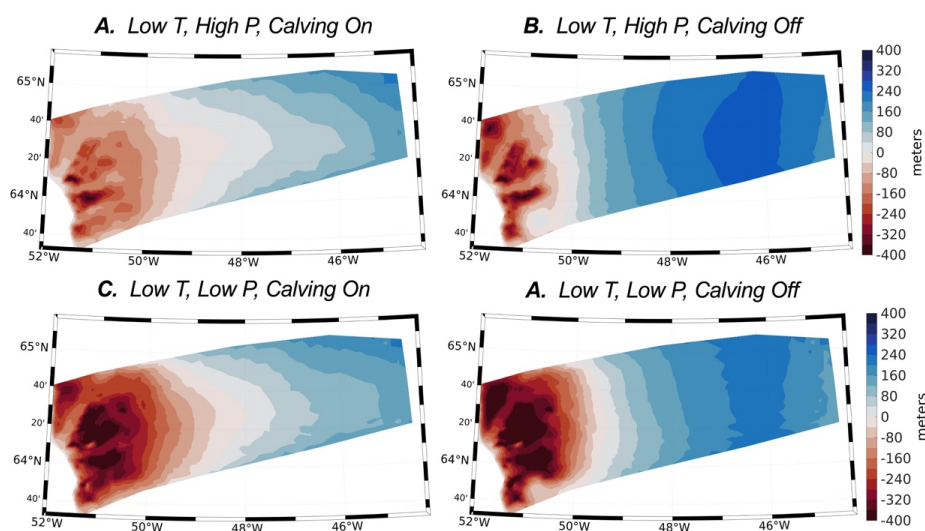


Figure 10. Simulated elevation changes during period 12ka-10ka shown for experiments using the low temperature forcing.

463
464
465
466
467

Reconstructions of Holocene ice thickness across the GrIS are limited, but ice-core records provide a long-term perspective of dynamic changes in GrIS elevation at locations at or near the ice divide (Vinther et al., 2009; Lecavalier et al., 2017). For example, some locations experienced more rapid thinning in response to Holocene warming (i.e. Camp Century, Dye 3) while other locations



468 experienced more muted ice elevation changes (i.e. GRIP, NGRIP). A feature of many of these
469 records, however, is the presence of early Holocene thickening, potentially triggered by increased
470 snowfall at higher elevation sites as the climate warmed or by elevation-mass balance feedbacks
471 driven by isostatic uplift (Vinther et al., 2009). Across all model experiments, our simulated timing
472 of inland thickening coincides with thickening experienced at high elevation ice core locations
473 (Vinther et al., 2009). The magnitude of early Holocene thickening from ice core records (Vinther
474 et al., 2009; 11.7 ka-10 ka) is on the order of 30 – 70 meters. Therefore, our simulations that allow
475 calving display inland thickening (<120 m) over the time interval 12 ka – 10 ka that is more
476 consistent with thickening estimated from ice cores than simulations with no calving (>200m).

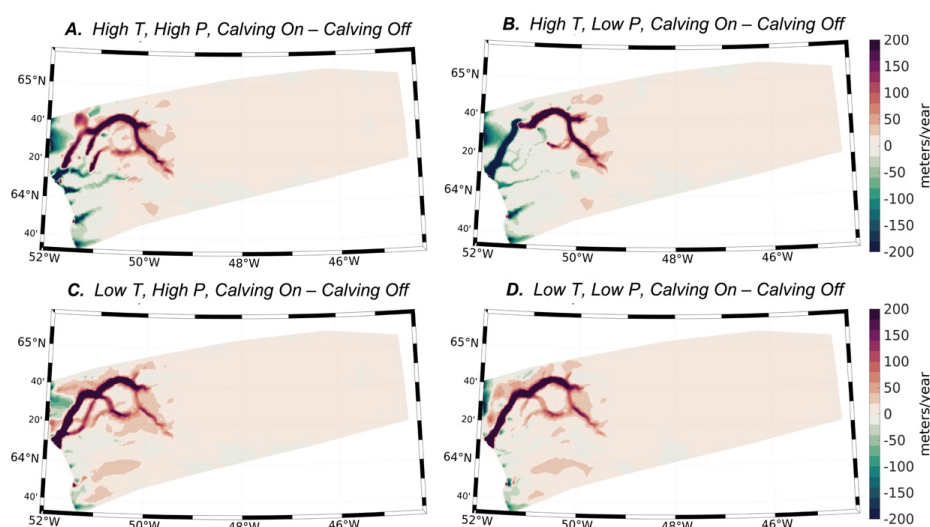


Figure 11. Simulated ice velocity differences between simulations with and without calving for each experiment over the time period 12 ka to 10 ka. Red colors denote an increase in ice velocity for simulations with calving relative to simulations without calving. Green colors denote a decrease in ice velocity for simulations with calving relative to simulations without calving.

477
478
479

4.4 Sensitivity to marine forcing

480 Experiments on the tensile strength of ice show that stress thresholds can vary between 150 kPa
481 and 3100 kPa (Petrovic, J., 2003), with modeling experiments on Jakobshavn glacier suggesting
482 that the stress threshold for grounded ice can vary between 100 kPa to 4 MPa seasonally (Bondzio
483 et al., 2017). Here, our grounded ice stress threshold is set to 600 kPa. Because our model setup
484 incurs large computational expense, we did not perform a full uncertainty analysis on these
485 parameterizations. Due to the nature of modeled variation in calibrated stress thresholds across
486 Greenland (Choi et al., 2021), however, we ran a small set of experiments where we set the calving
487 stress threshold on grounded ice to 1 MPa. We performed the transient simulations on the high
488 and low temperature scenario cases using the high precipitation forcing (see Table 1).
489 Additionally, we ran a set of experiments where the basal melt rate on floating ice was set to 120
490 m/yr. Figure 12 shows the simulated ice volumes for these experiments where the calving stress
491 threshold of grounded ice and basal melt rate on floating ice were changed. These experiments

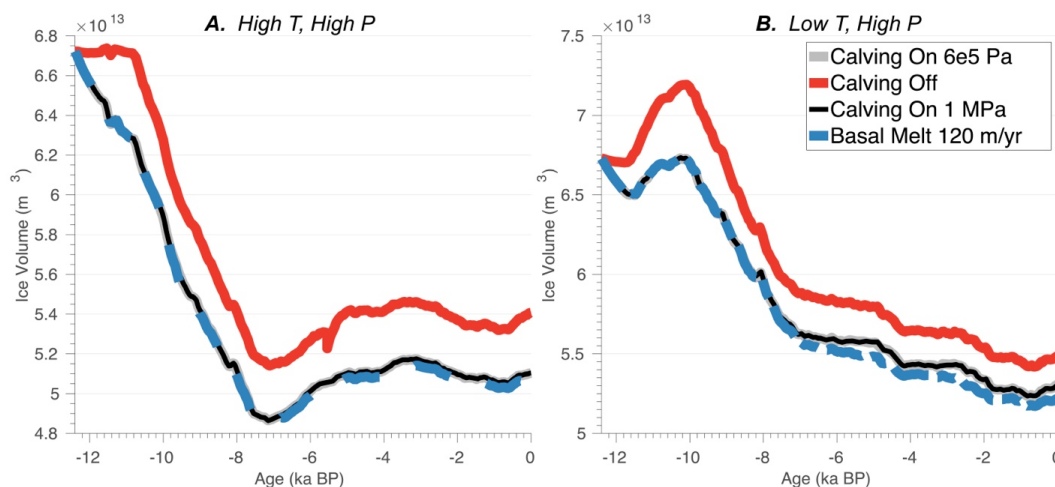


Figure 12. Sensitivity to the calving stress threshold for grounded ice and basal melt rates on floating ice. Red line: ice volume evolution for the simulations where the calving parameterization was turned off. Black line: ice volume evolution for the simulations where the calving stress threshold for grounded ice is 1 MPa. Gray line: ice volume evolution for the simulations where the calving stress threshold for grounded ice is 6 kPa. Dashed blue line: ice volume evolution for the simulations where the basal melt rate on floating ice was set to 120 m/yr (with calving stress threshold for grounded ice = 600 kPa).

492 reveal that adjusting the stress threshold from 600 kPa to 1 MPa has no effect on the evolution of
493 the simulated ice volume. Accordingly, increasing the basal melt rate on floating ice has minimal
494 effect on the simulated ice volume (Figure 12). Ice only begins to float in our experiments when
495 the ice front retreats into the deeper fjord bathymetry within the KNS forefield (see Figure 3), and
496 therefore submarine melting of floating ice seems to have limited influence on simulated ice mass
497 changes.

498

499 5. Discussion

500

501 5.1 Terrestrial vs. Marine ice retreat

502

503 Southwestern Greenland hosts a rich record of geologic constraints on past ice-sheet change
504 (Lesnek et al., 2020). Whereas a series of well-defined moraines constrain early Holocene ice
505 retreat across portions of southwestern Greenland dominated by terrestrial ice-margin settings
506 (Larsen et al., 2014; Lesnek et al., 2020; Young et al., 2020; Young et al., 2021), the Kapisigdlit
507 moraine system (Figure 2: early Holocene moraines) near the present-day ice margin is the only
508 regionally traceable moraine within the marine-dominated KNS forefield. Instead, ice-margin
509 retreat across the KNS forefield is constrained primarily by minimum limiting radiocarbon ages
510 and ¹⁰Be surface exposure ages on deglaciated bedrock surfaces and glacial erratics (Larsen et al.,
511 2014; Young et al., 2021). The lack of moraine systems between coast and ice is consistent with
512 the relatively high rate of deglaciation estimated from the existing chronology. These
513 chronological constraints detail widespread and rapid retreat of the ice margin across this domain
514 in the early Holocene, with the ice margin retreating from the coastline around 12 ka to near the
515 present-day ice margin between 10-9.5 ka (Young et al., 2021). This relatively rapid retreat based



516 on geological observation is consistent with the lack of elevation-age relationship in our
517 simulations of ice margin change.

518
519 While the rapid retreat of the terrestrial ice margin is well constrained, how ice retreated up the
520 fjords is less certain. Our simulations depict a pattern of ice retreat across the landscape that was
521 largely independent of ice retreat within fjords, which lagged by 0.5 – 2 ka. For our simulations,
522 scenarios using the same climate forcing show little difference (<1 ka) in the simulated age of ice
523 retreat on terrestrial ice margins regardless of whether calving is allowed (Figures 5 and 6). The
524 timing and rate of Holocene ice retreat across terrestrial portions of the KNS forefield, however,
525 is strongly dependent on the climate forcing used, and ultimately the SMB. The earliest ice retreat
526 occurs in simulations that use the high temperature scenario. Ice retreat occurs later in simulations
527 that use the low temperature scenario, which has a delay in the timing and magnitude of Holocene
528 warming (Figure 4). The pace and magnitude of ice retreat is shown to be modulated depending
529 on precipitation similar to the findings of Briner et al. (2020) and Downs et al. (2020), with delayed
530 and less rapid ice retreat in scenarios with higher precipitation (Figures 5a and 6a). These results
531 point to the strong influence that climate and, in particular, precipitation can have on modulating
532 the temperature driven response of Holocene deglaciation. Indeed, select proxy records suggest
533 that southwestern Greenland may have experienced a prolonged period of anomalously high
534 snowfall in the early Holocene, perhaps driven by increased moisture flux from Baffin Bay and
535 the Labrador Sea as sea-ice extent declined (Thomas et al., 2016). Ice flow modeling across
536 southwestern Greenland has also revealed that elevated precipitation may have accompanied early
537 Holocene warming (Downs et al., 2020). And recent evidence from a shallow ice core in western
538 Greenland reveal that significant variations in precipitation occurred in the last two thousand years
539 across the margins of the GrIS, whereas this variability is not present in ice core data at the interior
540 of the GrIS (Osman et al., 2021). Because current climate reconstructions employed in
541 paleoclimate ice flow modeling use either simple scaling approaches to reconstruct past climate or
542 rely on information from interior ice cores, large hydroclimate shifts that occur at the ice sheet
543 margin may not be captured (Badgeley et al., 2020). Continued progress in reconstructing past
544 climate will certainly improve our understanding of climatic controls on the long-term response of
545 the GrIS.

546
547 In general, simulations using the high temperature scenario experience terrestrial ice retreat that
548 occurs during 11.5 ka to 9 ka, a time window consistent with the geological record of ice-margin
549 change in our domain (Larsen et al., 2014; Young et al., 2021). Simulations using the low
550 temperature scenario reveal terrestrial ice retreat also beginning ca. 11.5 ka, but deglaciation of
551 our model domain continues until ~7.5 ka. In comparison, geological constraints suggest that by
552 ~10.3-9 ka BP the ice margin in the immediate KNS region had already retreated back to, and
553 likely behind, what is the present-day ice margin (Young et al., 2021). Ice surface lowering is
554 captured in all of our simulations, which indicate that on terrestrial surfaces ice retreat was
555 synchronous across low and high elevations. While ice calving does not seem to significantly
556 influence the rate and timing of ice retreat across terrestrial portions of our domain, late Holocene
557 ice readvance within fjords is more restricted in those simulations that use the calving
558 parametrization. Accordingly, flowband modeling of KNS over the period historical period of
559 1761 to 2012 suggests that marine ice-front retreat was primarily influenced by atmospheric
560 warming and runoff, which helped to trigger ice front retreat via a crevasse-depth calving criterion,
561 with submarine melting only playing a minor role on historical retreat (Lea et al., 2014; Lea et al.,



562 2014). These results do suggest though that climate anomalies were the main driver of historical
563 ice terminus advance and retreat across KNS (Lea et al, 2014), with our results suggesting that the
564 longer-term Holocene ice terminus position was also primarily driven by atmospheric warming
565 and not through oceanic melting.

566 **5.2 Role of ice calving on mass transport**

567
568
569 Mass transport from the ice sheet interior to the margin plays an important role in ice sheet mass
570 change and ultimately its contribution to sea-level rise. Contemporary satellite-derived
571 measurements show inland thickening at high elevations across portions of the GrIS in response
572 to increased snowfall despite pervasive thinning at lower elevations (Smith et al., 2020). Although
573 the response of marine terminating portions of the GrIS and how it translates to interior ice mass
574 loss can be spatially varying (Williams et al., 2021), thinning at the ice margin due to dynamic- or
575 SMB-driven ice loss can elicit changes in driving stresses, which can propagate up glacier and into
576 the interior of the ice sheet (Price et al., 2008; Schlegel et al., 2013; Csatho et al., 2014; Felikson
577 et al., 2020; Williams et al., 2021).

578
579 While there is no apparent influence of ice calving on the Holocene ice retreat across the KNS
580 forefield over terrestrial surfaces, our simulations show that ice calving has a significant influence
581 on the evolution of the total ice volume. Ultimately, ice calving leads to an acceleration of ice
582 flow within outlet glaciers that promotes local ice thinning first, followed by propagation of this
583 thinning into the interior of the ice sheet, consistent with contemporary observations (Csatho et
584 al., 2014; Williams et al., 2021). Initially, interior ice surface elevation increases in our
585 simulations, with simulations that allow calving being more consistent with ice-core derived
586 surface height records (Vinther et al., 2009). Surface lowering near the ice margin driven by a
587 more negative SMB in response to early Holocene warming causes the ice surface slopes to steepen
588 in our domain, increasing driving stresses and mass transport. This helps drive interior ice
589 thinning, as shown by elevation changes in simulations that allow ice calving (Figures 9 and 10),
590 leading to increased ice flux at the margin through the ice streams (Figure 11). This increased
591 mass transport helps limit thinning within outlet glaciers, and where terrestrial locations of our
592 domain become ice free early in the Holocene, ice front retreat within the fjords lag (Figure 5 and
593 6).

594
595 Our results suggest that, while calving did not play a significant role in the observed Holocene ice
596 retreat across the KNS forefield, it played an important role on the overall ice mass change across
597 our model domain. These results highlight that the inclusion of physically based ice calving
598 parameterizations is an important step towards modeling the fidelity of simulated ice mass change
599 across paleoclimate timescales. However, the choice of which ice calving parameterization is best
600 suited to Greenland over such timescales is still not well constrained (Goelzer et al., 2017). It
601 remains important though, that models maintain high enough spatial resolution in order to capture
602 fjord environments, associated bathymetry, and ultimately ice calving and grounding line
603 migrations over paleoclimate timescales (Cuzzone et al., 2019) as the model resolution can impact
604 simulated ice discharge significantly (Rückamp et al., 2020; Ashwanden et al., 2019).

605 **5.3 Model limitations**

606
607



608 Fjord systems in Greenland are typically <5 km in width, making it necessary to implement high-
609 resolution meshes to resolve these features. Our model setup relies on a high-resolution mesh that
610 is able to capture the fjord geometry within the KNS forefield, making it possible to simulate
611 grounding line migration and calving. The calving parameterization used does ignore frontal
612 melting at the grounded ice front. Frontal melt at the base of a calving face has been shown to
613 induce undercutting of the ice front, and greatly increases calving rates (O’leary and
614 Christofferson, 2013). For the present day, many of southwestern Greenland’s marine terminating
615 glaciers are not strongly influenced by undercutting (Wood et al., 2021), but this may have been
616 different as ice retreated up fjord to its present-day location through the Holocene. Due to a lack
617 of constraints on the long term subsurface ocean thermal forcing needed to implement undercutting
618 in our simulations, we opted to disregard this. To circumvent this shortcoming, we set our calving
619 stress threshold on grounded ice to a number (600 kPa) that is on the lower end of measured tensile
620 stresses of ice (Petrovic, 2003). Since there was no discernable difference in our simulated ice
621 mass change when a higher calving stress threshold of grounded ice was used (1 MPa), we
622 cautiously assume that implementation of undercutting would have a negligible effect on the
623 calving rates and overall Holocene mass change and ice retreat across our domain.

624
625 At the time of this work, ISSM is undergoing improvements and new implementation of solid earth
626 and sea-level feedbacks. While we did not include time dependent forcings (e.g. Caron et al.,
627 2018) that account for relative sea-level change as we have in prior research (Cuzzone et al., 2019;
628 Briner et al., 2020), future simulations using ISSM will explore the influence of coupled solid
629 Earth-ice feedbacks on ice retreat. Recent ice sheet modeling (Kajanto et al., 2020) showed that
630 the Holocene retreat of Jakobshavn Isbræ was insensitive to relative sea-level (RSL) variations, as
631 RSL changes were small in comparison to fjord depth. RSL changes during the Holocene across
632 this domain were relatively small (~60-100 meters at 12.4 ka and decreasing through the Holocene;
633 Caron et al., 2018) compared to fjord depths. Given that ice calving did not seem to largely
634 influence terrestrial ice retreat, we only expect that inclusion of Holocene RSL changes may have
635 influenced ice front retreat that migrated into deeper waters where floating extensions of the ice
636 front could occur. However, in our sensitivity tests, basal melting on floating ice plays a trivial
637 role in total ice volume changes (Figure 11) as most of the ice within fjords is grounded during the
638 Holocene retreat.

639 640 **6. Conclusions**

641
642 Understanding how climate, calving, and marine processes contribute to ice sheet change across
643 paleoclimate timescales is challenging. Models with lower resolution meshes are typically favored
644 to ensure computational needs are satisfied. This ultimately leads to poor representation of
645 bedrock topography (Cuzzone et al., 2019; Jones et al., 2021) and grounding line migration
646 (Seroussi et al., 2018) that control ice flow (i.e., fjords), making the assessment of how ice calving
647 influences large scale ice margin change difficult. Moreover, while ice core records provide
648 snapshots of a changing climate at the ice-sheet interior, there remain a relative lack of
649 paleoclimate records from the ice sheet margin of sufficient resolution that can be easily
650 incorporated into an ice sheet model’s climate forcing.

651
652 Here, we presented results from a high-resolution 3D thermomechanical regional ice sheet model
653 that evaluated controls on the behavior of the southwestern GrIS during the Holocene in the



654 vicinity of the KNS forefield, an area with extensive geologic constraints on past ice margin
655 change. Experiments were driven by novel reconstructions of Holocene climate (Badgeley et al.,
656 2020) and included a physically based ice calving parametrization (Morlighem et al., 2016).

657
658 Our modeling results shed light on the well constrained observations of Holocene ice retreat across
659 the KNS forefield. Our simulations agree well with observations that ice retreat on terrestrial
660 bedrock surfaces occurred rapidly between 11.5 ka to 9.5 ka in response to early Holocene
661 warming. Variations in the timing and magnitude of ice retreat on terrestrial bedrock surfaces
662 across this region are insensitive to calving within the fjords that intersect this landscape, and is
663 instead more sensitive to the SMB with warmer climate reconstructions providing the best fit
664 between the modeled and observed ice retreat. Calving across this domain plays a significant role
665 in the simulated Holocene ice volume change. Acting as conduits for mass transport and ice flux,
666 ice velocity within the fjords in the KNS forefield increases when the ice front is allowed to calve.
667 Calving helps promote further ice mass transport from the interior of the domain to the ice front.
668 This helps to thicken ice within the fjords, allowing the ice front to persist longer than adjacent
669 terrestrial margins similar to the ice response simulated for the Holocene retreat of Jakobshavn
670 Isbræ (Kajanto et al., 2020). However, as all simulations depict contemporary ice extent that is
671 too extensive, uncertainties in the reconstruction of past climate and model parametric
672 uncertainties ultimately contribute to misfits that are difficult to quantify given our
673 computationally expensive model setup. Future paleoclimate ice flow modelling with ISSM will
674 aim to take advantage of recent advances in statistical emulation (e.g., Edwards et al., 2021) to
675 better quantify the influence of model parametric uncertainty on simulated Holocene ice retreat.

676
677 Geologic archives serve an important role in our understanding of glacier and ice sheet response
678 to climate change. In turn, ice sheet modeling can help improve our understanding of the climatic
679 and ice dynamical factors that led to ice sheet changes preserved by the geologic record. Our
680 modeling results present an exploration of the factors that may have contributed to the observed
681 pattern of Holocene ice retreat across the KNS forefield, echoing that model–data comparisons
682 between ice sheet models and geologic reconstructions can help improve our understanding of
683 long-term ice sheet sensitivity to climatic and dynamic forcing mechanisms.

684 685 **Data Availability**

686
687 The simulations performed for this paper made use of the open-source Ice Sheet System Model
688 (ISSM) version 4.19 and are publicly available at <https://issm.jpl.nasa.gov/> (Larour et al., 2012).

689 690 **Acknowledgements**

691
692 Funding for this study was provided by the National Science Foundation Grant ARC
693 no. 2105960 to JC and no. 1503959 to NEY.

694 695 **References**

696
697 Aschwanden, A., Bueler, E., Khroulev, C., and Blatter, H.: An enthalpy formulation for glaciers
698 and ice sheets, *J. Glaciol.*, 58, 441–457, <https://doi.org/10.3189/2012JoG11J088>, 2012.
699 Aschwanden, A., Fahnestock, M.A., Truffer, M., Brinkerhoff, D.J., Hock, R., Khroulev, C.,



- 700 Mottram, R., Khan, S.A. Contribution of the Greenland Ice Sheet to sea level over the
701 next millennium. *Science Advances*. 5. DOI: 10.1126/sciadv.aav9396. 2019.
- 702 Åkesson, H., Morlighem, M., Nisancioglu, K. H., Svendsen, J. J., and Mangerud, J.:
703 Atmosphere-driven ice sheet mass loss paced by topography: Insights from modelling the
704 south-western Scandinavian Ice Sheet, *Quaternary Sci. Rev.*, 195, 32–
705 47, <https://doi.org/10.1016/j.quascirev.2018.07.004>, 2018.
- 706 Badgeley, J. A., Steig, E. J., Hakim, G. J., and Fudge, T. J.: Greenland temperature and
707 precipitation over the last 20 000 years using data assimilation, *Clim. Past*, 16, 1325–
708 1346, <https://doi.org/10.5194/cp-16-1325-2020>, 2020.
- 709 Blatter, H.: Velocity and stress-fields in grounded glaciers: A simple algorithm for including
710 deviatoric stress gradients, *J. Glaciol.*, 41, 333, 344
711 <https://doi.org/10.3189/S002214300001621X>, 1995.
- 712 Box, J. E.: Greenland ice sheet mass balance reconstruction. Part II: Surface mass balance
713 (1840–2010), *J. Clim.*, 26, 6974–6989, <https://doi.org/10.1175/JCLI-D-12-00518.1>, 2013.
- 714 Briner, J. P., McKay, N., Axford, Y., Bennike, O., Bradley, R. S., de Vernal, A., Fisher, D. A.,
715 Francus, P., Fréchette, B., Gajewski, K. J., Jennings, A. E., Kaufman, D. S., Miller, G.
716 H., Rouston, C., and Wagner, B.: Holocene climate change in Arctic Canada and
717 Greenland, *Quaternary Sci. Rev.*, 147, 340–364, 2016.
- 718 Briner, J. P., Cuzzone, J. K., Badgeley, J. A., Young, N. E., Steig, E. J., Morlighem, M.,
719 Schlegel, N.-J., Hakim, G., Schaefer, J. Johnson, J. V., Lesnek, A. L., Thomas, E. K.,
720 Allan, E., Bennike, O., Cluett, A. A., Csatho, B., de Vernal, A., Downs, J., Larour, E.,
721 and Nowicki, S.: Rate of mass loss from the Greenland Ice Sheet will exceed Holocene
722 values this century, *Nature*, 6, 70–74, <https://doi.org/10.1038/s41586-020-2742-6>, 2020.
- 723 Bondzio, J. H., Seroussi, H., Morlighem, M., Kleiner, T., Rückamp, M., Humbert, A., and
724 Larour, E. Y.: Modelling calving front dynamics using a level-set method: application to
725 Jakobshavn Isbræ, West Greenland, *The Cryosphere*, 10, 497–510,
726 <https://doi.org/10.5194/tc-10-497-2016>, 2016.
- 727 Bondzio, J., Morlighem, M., Seroussi, H., Kleiner, T., Rückamp, M., Mouginot, J., Moon, T.,
728 Larour, E., Humbert, A. The mechanisms behind Jakobshavn Isbrae’s acceleration and
729 mass loss: a 3-D thermomechanical model study. *Geophys. Res. Lett.*, 44 (12) pp. 6252–
730 6260, 10.1002/2017GL073309, 2017
- 731 Caron, L., Ivins, E. R., Larour, E., Adhikari, S., Nilsson, J., and Blewitt, G.: GIA model statistics
732 for GRACE hydrology, cryosphere and ocean science, *Geophys. Res. Lett.*, 45, 2203–
733 2212, <https://doi.org/10.1002/2017GL076644>, 2018.
- 734 Choi, Y., Morlighem, M., Rignot, E. *et al.* Ice dynamics will remain a primary driver of
735 Greenland ice sheet mass loss over the next century. *Commun Earth Environ* 2, 26.
736 <https://doi.org/10.1038/s43247-021-00092-z>, 2021
- 737 Courant, R., Friedrichs, K. & Lewy, H. Über die partiellen Differenzgleichungen der
738 mathematischen Physik. *Math. Ann.* 100, 32–74, 1928
- 739 Cuffey, K. M. and Paterson, W. S. B.: The physics of glaciers, 4th edn., Butterworth-Heinemann,
740 Oxford, 2010.
- 741 Cuzzone, J., Morlighem, M., Larour, E., Schlegel, N., and Seroussi, H.: Implementation of
742 higher-order vertical finite elements in ISSM v4.13 for improved ice sheet flow modeling over
743 paleoclimate timescales, *Geosci. Model Dev.*, 11, 1683–
744 1694, <https://doi.org/10.5194/gmd-11-1683-2018>, 2018.
- 745 Cuzzone, J. K., Schlegel, N.-J., Morlighem, M., Larour, E., Briner, J. P., Seroussi, H., and Caron,



- 746 L.: The impact of model resolution on the simulated Holocene retreat of the southwestern
747 Greenland ice sheet using the Ice Sheet System Model (ISSM), *The Cryosphere*, 13, 879–
748 893, <https://doi.org/10.5194/tc-13-879-2019>, 2019.
- 749 Csatho, B.M., Schenk, A.F., van der Veen, C., Babonis, G., Duncan, K., Rezvanbehbahani, S.,
750 van den Broecke, M.R., Simonsen, S.B., Nagarajan, S., van Angelen, J.H. Laser
751 altimetry reveals complex pattern of Greenland ice sheet dynamics. *Proceedings of the*
752 *National Academy of Sciences* 111, 18478–18483, 2014
- 753 Downs, J., Johnson, J., Briner, J., Young, N., Lesnek, A., and Cuzzone, J.: Western Greenland
754 ice sheet retreat history reveals elevated precipitation during the Holocene thermal
755 maximum, *The Cryosphere*, 14, 1121–1137, <https://doi.org/10.5194/tc-14-1121-2020>,
756 2020.
- 757 Edwards, T. L., Nowicki, S., Marzeion, B., Hock, R., Goelzer, H., Seroussi, H., Jourdain,
758 N. C., Slater, D. A., Turner, F. E., Smith, C. J., McKenna, C. M., Simon, E., Abe-Ouchi,
759 A., Gregory, J. M., Larour, E., Lipscomb, W. H., Payne, A. J., Shepherd, A., Agosta, C.,
760 Alexander, P., Albrecht, T., Anderson, B., Asay-Davis, X., Aschwanden, A., Barthel, A.,
761 Bliss, A., Calov, R., Chambers, C., Champollion, N., Choi, Y., Cullather, R., Cuzzone, J.,
762 Dumas, C., Felikson, D., Fettweis, X., Fujita, K., Galton-Fenzi, B. K., Gladstone, R.,
763 Gollledge, N. R., Greve, R., Hattermann, T., Hoffman, M. J., Humbert, A., Huss, M.,
764 Huybrechts, P., Immerzeel, W., Kleiner, T., Kraaijenbrink, P., Le clec’h, S., Lee, V.,
765 Leguy, G. R., Little, C. M., Lowry, D. P., Malles, J.-H., Martin, D. F., Maussion, F.,
766 Morlighem, M., O’Neill, J. F., Nias, I., Pattyn, F., Pelle, T., Price, S. F., Quiquet, A.,
767 Radić, V., Reese, R., Rounce, D. R., Rückamp, M., Sakai, A., Shafer, C., Schlegel, N.-J.,
768 Shannon, S., Smith, R. S., Straneo, F., Sun, S., Tarasov, L., Trusel, L. D., Van Breedam,
769 J., van de Wal, R., van den Broeke, M., Winkelmann, R., Zekollari, H., Zhao, C., Zhang,
770 T., and Zwinger, T.: Projected land ice contributions to twenty-first-century sea level rise,
771 *Nature*, 593, 74–82, <https://doi.org/10.1038/s41586-021-03302-y>, 2021.
- 772 Felikson, D., Catania, G., Bartholomäus, T.C., Morlighem, M and Noël, B. Steep glacier bed
773 knickpoints mitigate inland thinning in Greenland. *Geophysical Research Letters*.
774 doi: 10.1029/2020GL090112, 2020
- 775 He, F., Shakun, J. D., Clark, P. U., Carlson, A. E., Liu, Z., Otto-Bliesner, B. L., and Kutzbach,
776 J. E.: Northern Hemisphere forcing of Southern Hemisphere climate during the last
777 deglaciation, *Nature*, 494, 81–85, [10.1038/nature11822](https://doi.org/10.1038/nature11822), 2013
- 778 Howat, I. M., Negrete, A., and Smith, B. E.: The Greenland Ice Mapping Project (GIMP) land
779 classification and surface elevation datasets, *The Cryosphere*, 8, 1509–
780 1518, <https://doi.org/10.5194/tc-8-1509-2014>, 2014.
- 781 IMBIE Team. Mass balance of the Greenland Ice Sheet from 1992 to 2018. *Nature*, 579
782 (7798) pp. 233–239. [10.1038/s41586-019-1855-2](https://doi.org/10.1038/s41586-019-1855-2), 2019
- 783 Enderlin, E. M., Howat, I. M., Jeong, S., Noh, M. J., van Angelen, J. H., & van den Broeke, M.
784 R.
785 An improved mass budget for the Greenland ice sheet. *Geophysical Research Letters*, 41,
786 866–872. <https://doi.org/10.1002/2013GL059010>. 2014
- 787 Vizcaino, M. Ice sheets as interactive components of Earth System Models: Progress and
788 challenges. *Wiley Interdisciplinary Reviews: Climate Change*, 5(4), 557–568.
789 <https://doi.org/10.1002/wcc.285>, 2014
- 790 Goelzer, H., Robinson, A., Seroussi, H. *et al.* Recent Progress in Greenland Ice Sheet



- 791 Modelling. *Curr Clim Change Rep* 3, 291–302 <https://doi.org/10.1007/s40641-017-0073->
792 y, 2017
- 793 Goelzer, H., Nowicki, S., Payne, A., Larour, E., Seroussi, H., Lipscomb, W. H., Gregory, J.,
794 Abe-
795 Ouchi, A., Shepherd, A., Simon, E., Agosta, C., Alexander, P., Aschwanden, A., Barthel,
796 A., Calov, R., Chambers, C., Choi, Y., Cuzzone, J., Dumas, C., Edwards, T., Felikson,
797 D., Fettweis, X., Gollede, N. R., Greve, R., Humbert, A., Huybrechts, P., Le clec'h, S.,
798 Lee, V., Leguy, G., Little, C., Lowry, D. P., Morlighem, M., Nias, I., Quiquet, A.,
799 Rückamp, M., Schlegel, N.-J., Slater, D., Smith, R., Straneo, F., Tarasov, L., van de Wal,
800 R., and van den Broeke, M.: The future sea-level contribution of the Greenland ice sheet:
801 a multi-model ensemble study of ISMIP6, *The Cryosphere*, <https://doi.org/10.5194/tc->
802 2019-319, 2020.
- 803 Fettweis, X., Hanna, E., Gallée, H., Huybrechts, P., & Erpicum, M. Estimation of the
804 Greenland ice sheet surface mass balance for the 20th and 21st centuries. *The*
805 *Cryosphere*, 2(2), 117–129. <https://doi.org/10.5194/tc-2-117-2008>, 2008
- 806 Janssens, I., and P. Huybrechts. The treatment of meltwater retention in mass-balance
807 parameterizations of the Greenland ice sheet, *Ann. Glaciol.*, 31, 133– 140.
808 [10.3189/172756400781819941](https://doi.org/10.3189/172756400781819941), 2000
- 809 Jones, R.S., Whitmore, R.J., Mackintosh, A.N., Norton, K.P, Eaves, S.R, Stutz, J., Christl, M.
810 Regional-scale abrupt Mid-Holocene ice sheet thinning in the western Ross Sea,
811 Antarctica. *Geology*, 49 (3): 278–282. doi: <https://doi.org/10.1130/G48347.1>, 2020
- 812 Kajanto, K., Seroussi, H., de Fleurian, B., Nisancioglu, K.H. Present day Jakobshavn
813 Isbræ (West Greenland) close to the Holocene minimum extent. *Quaternary Science*
814 *Reviews*, 24, <https://doi.org/10.1016/j.quascirev.2020.106492>, 2020
- 815 Larour, E., Seroussi, H., Morlighem, M., and Rignot, E.: Continental scale, high order, high
816 spatial resolution, ice sheet modeling using the Ice Sheet System Model (ISSM), *J.*
817 *Geophys. Res.-Earth*, 117, F01022, <https://doi.org/10.1029/2011JF002140>, 2012.
- 818 Larsen, N. K., Funder, S., Kjær, K. H., Kjeldsen, K. K., Knudsen, M. F., and Linge, H.: Rapid
819 early Holocene ice retreat in West Greenland, *Quaternary Sci. Rev.*, 92, 310–
820 323, <https://doi.org/10.1016/j.quascirev.2013.05.027>, 2014.
- 821 Lecavalier, B. S., Milne, G. A., Simpson, M. J. R., Wake, L., Huybrechts, P., Tarasov, L.,
822 Kjeldsen, K. K., Funder, S., Long, A. J., Woodroffe, S., Dyke, A. S., and Larsen, N. K.:
823 A model of Greenland ice sheet deglaciation constrained by observations of relative sea
824 level and ice extent, *Quaternary Sci. Rev.*, 102, 54–
825 84, <https://doi.org/10.1016/j.quascirev.2014.07.018>, 2014.
- 826 Lea, J. M., Mair, D. W. F., Nick, F. M., Rea, B. R., van As, D., Morlighem, M., Nienow, P. W.,
827 and Weidick, A.: Fluctuations of a Greenlandic tidewater glacier driven by changes in
828 atmospheric forcing: observations and modelling of Kangiata Nunaata Sermia, 1859–
829 present, *The Cryosphere*, 8, 2031–2045, <https://doi.org/10.5194/tc-8-2031-2014>, 2014.
- 830 Lea, J. M., Mair, D. W. F., Nick, F. M., Rea, B. R., Weidick, A., Kjær, K. H., Morlighem, M.,
831 van As, D., and Schofield, J. E.: Terminus-driven retreat of a major southwest Greenland
832 tidewater glacier during the early 19th century: insights from glacier reconstructions and
833 numerical modelling, *J. Glaciol.*, 60, 333–344, <https://doi.org/10.3189/2014JoG13J163>,
834 2014.
- 835 Lecavalier, B. S., Fisher, D. A., Milne, G. A., Vinther, B. M., Tarasov, L., Huybrechts, P.,



- 836 Lacelle, D., Main, B., Zheng, J., Bourgeois, J., and Dyke, A. S.: High Arctic Holocene
837 temperature record from the Agassiz ice cap and Greenland ice sheet evolution, *P. Natl.*
838 *Acad. Sci. USA*, 23, 5952–5957, <https://doi.org/10.1073/pnas.1616287114>, 2017.
- 839 Le Morzadec, K., Tarasov, L., Morlighem, M., and Seroussi, H. 2015. A new sub-grid surface
840 mass balance and flux model for continental-scale ice sheet modelling: testing and last
841 glacial cycle, *Geosci. Model Dev.*, 8, 3199–3213, [https://doi.org/10.5194/gmd-8-3199-](https://doi.org/10.5194/gmd-8-3199-2015)
842 2015.
- 843 Lenaerts, J. T. M., Medley, B., van den Broeke, Michiel R., & Wouters, B. Observing and
844 modeling Ice-Sheet surface mass balance. *Reviews of Geophysics*, 57(2), 376–420.
845 doi:10.1029/2018RG000622, 2019.
- 846 Lesnek, A. J., Briner, J. P., Young, N. E., and Cuzzone, J. K.: Maximum southwest Greenland
847 Ice Sheet recession in the early Holocene, *Geophys. Res. Lett.*, 47,
848 e2019GL083164, <https://doi.org/10.1029/2019GL083164>, 2020.
- 849 Liu, Z., Otto-Bliesner, B., He, F., Brady, E., Tomas, R., Clark, P., Carlson, A., Lynch-Stieglitz,
850 J., Curry, W., Brook, E., Erickson, D., Jacob, R., Kutzbach, J., and Cheng, J.: Transient
851 simulation of last deglaciation with a new mechanism for Bølling-Allerød warming,
852 *Science*, 325, 310–314, <https://doi.org/10.1126/science.1171041>, 2009
- 853 Morlighem, M., Rignot, E., Seroussi, H., Larour, E., Ben Dhia, H., and Aubry, D.: Spatial
854 patterns of basal drag inferred using control methods from a full-Stokes and simpler
855 models for Pine Island Glacier, West Antarctica, *Geophys. Res. Lett.*, 37,
856 L14502, <https://doi.org/10.1029/2010GL043853>, 2010.
- 857 Morlighem, M., Bondzio, J., Seroussi, H., Rignot, E., Larour, E., Humbert, A.,
858 Rebuffi, S., Modeling of Store Gletscher's calving dynamics, West Greenland, in
859 response to ocean thermal forcing, *Geophys. Res. Lett.*, 43,
860 doi:10.1002/20116GL067695, 2016
- 861 Morlighem, M., Williams, C. N., Rignot, E., An, L., Arndt, J. E., Bamber, J. L., Catania, G.,
862 Chauché, N., Dowdeswell, J. A., Dorschel, B., Fenty, I., Hogan, K., Howat, I., Hubbard,
863 A., Jakobsson, M., Jordan, T. M., Kjeldsen, K. K., Millan, R., Mayer, L., Mouginot, J.,
864 Noël, B. P. Y., Ó Cofaigh, C., Palmer, S., Rysgaard, S., Seroussi, H., Siegert, M. J.,
865 Slabon, P., Straneo, F., van den Broeke, M. R., Weinrebe, W., Wood, M., and Zinglensen,
866 K. B.: BedMachine v3: Complete bed topography and ocean bathymetry mapping of
867 Greenland from multi-beam echo sounding combined with mass conservation, *Geophys.*
868 *Res. Lett.*, 44, 11051–11061, <https://doi.org/10.1002/2017GL074954>, 2017
- 869 O'Leary, M. and Christoffersen, P.: Calving on tidewater glaciers amplified by submarine frontal
870 melting, *The Cryosphere*, 7, 119–128, <https://doi.org/10.5194/tc-7-119-2013>, 2013.
- 871 Osman, M.B., Smith, B.E., Trusel, L.D., Das, S.B., McConnell, J.R., Chellman, N., Arienzo, M.,
872 Sodemann, H. Abrupt Common Era hydroclimate shifts drive west Greenland ice cap
873 change. *Nat. Geosci.* 14, 756–761 (2021). <https://doi.org/10.1038/s41561-021-00818-w>
- 874 Pattyn, F.: A new three-dimensional higher-order thermomechanical ice sheet model: Basic
875 sensitivity, ice stream development, and ice flow across subglacial lakes, *J. Geophys.*
876 *Res.*, 108, 2382, <https://doi.org/10.1029/2002JB002329>, 2003
- 877 Petrovic, J. J. Review Mechanical properties of ice and snow. *J. Mater. Sci.* 38, 1–6, 2003
- 878 Price, SF, Payne, AJ, Catania, GA and Neumann, TA. Seasonal acceleration of inland ice via
879 longitudinal coupling to marginal ice. *Journal of Glaciology* 54(185), 213–219, 2008
- 880 Rignot, E. and Mouginot, J.: Ice flow in Greenland for the international polar year 2008–2009,
881 *Geophys. Res. Lett.*, 39, L11501, <https://doi.org/10.1029/2012GL051634>, 2012.



- 882 Rückamp, M., Greve, R., Humbert, A. Comparative simulations of the evolution of the
883 Greenland ice sheet under simplified Paris Agreement scenarios with the models
884 SICOPOLIS and ISSM. *Polar Science*. 21, 14-25.
885 <https://doi.org/10.1016/j.polar.2018.12.003>. 2019.
- 886 Schlegel, N.J., Larour, E., Seroussi, H., Morlighem, M., Box, J.E., Decadal-scale sensitivity of
887 northeast Greenland ice flow to errors in surface mass balance using ISSM. *J. Geophys.*
888 *Res. - Earth Surface*, 118, doi: 10.1002/jgrf.20062. 2013.
- 889 Seroussi, H. and Morlighem, M.: Representation of basal melting at the grounding line in ice
890 flow models, *The Cryosphere*, 12, 3085–3096, <https://doi.org/10.5194/tc-12-3085-2018>.
891 2018
- 892 Shapiro, N. M. and Ritzwoller M. H.: Inferring surface heat flux distribution guided by a global
893 seismic model: particular application to Antarctica, *Earth Planet. Sc. Lett.*, 223, 213–
894 224, <https://doi.org/10.1016/j.epsl.2004.04.011>, 2004.
- 895 Smith B, Fricker HA, Gardner AS, Medley B, Nilsson J, Paolo FS, Holschuh N, Adusumilli S,
896 Brunt K, Csatho B, Harbeck K, Markus T, Neumann T, Siegfried MR, Zwally HJ.
897 Pervasive ice sheet mass loss reflects competing ocean and atmosphere processes.
898 *Science*. 368(6496):1239-1242. doi: 10.1126/science.aaz5845, 2020
- 899 Smith-Johnsen, S., Schlegel, N.-J., de Fleurian, B., & Nisancioglu, K. H. Sensitivity of the
900 Northeast Greenland Ice Stream to geothermal heat. *Journal of Geophysical Research:*
901 *Earth Surface*, 125, e2019JF005252. <https://doi.org/10.1029/2019JF005252>, 2020
- 902 Thomas, E. K., Briner, J. P., Ryan-Henry, J. J., and Huang, Y.: A major increase in winter
903 snowfall during the middle Holocene on western Greenland caused by reduced sea ice in
904 Baffin Bay and the Labrador Sea, *Geophys. Res. Lett.*, 43, 5302–
905 5308, <https://doi.org/10.1002/2016GL068513>, 2016
- 906 Vinther, B., Buchardt, S., Clausen, H. *et al.* Holocene thinning of the Greenland ice
907 sheet. *Nature* 461, 385–388, <https://doi.org/10.1038/nature08355>, 2009
- 908 Weidick, A., Bennike, O., Citterio, M., and Nøgaard-Pedersen, N.: Neoglacial and historical
909 glacier changes around Kangarsuneq fjord in southern West Greenland, *Geol. Surv. Den.*
910 *Greenla.*, 27, 1-68. <https://doi.org/10.34194/geusb.v27.4694>, 2012.
- 911 Williams, J. J., Gourmelen, N., Nienow, P. Complex multi-decadal ice dynamical change inland
912 of marine-terminating glaciers on the Greenland Ice Sheet. *Journal of Glaciology*. 1-14.
913 <https://doi.org/10.1017/jog.2021.31>, 2021
- 914 Wood, M., Rignot, E., Fenty, I., An, L., Bjørk, A., van den Broeke, M., Cai, C., Kane, E.,
915 Menemenlis, D., Millan, R., Morlighem, M., Mouginot, J., Noël, B., Scheuchl, B.,
916 Velicogna, I., Willis, J. K., & Zhang, H. Ocean forcing drives glacier retreat in
917 Greenland. *Science Advances*, 7(1), <https://doi.org/10.1126/sciadv.aba7282>, 2021
- 918 Young, N. E. and Briner, J. P.: Holocene evolution of the western Greenland Ice Sheet:
919 Assessing geophysical ice-sheet models with geological reconstructions of ice-margin
920 change, *Quaternary Sci. Rev.*, 114, 1-17, <https://doi.org/10.1016/j.quascirev.2015.01.018>,
921 2015.
- 922 Young, N.E., Briner, J.P., Miller, G.H., Lesnek, A.J., Crump, S.E., Thomas, E.K., Pendleton,
923 S.L., Cuzzone, J., Lamp, J., Zimmerman, S., Caffee, M., Schaefer, J.M., 2020.
924 Deglaciation of the Greenland and Laurentide ice sheets interrupted by glacier advance
925 during abrupt coolings. *Quat. Sc. Rev.* 229, 106091.
- 926 Young, N. E., Lesnek, A. J., Cuzzone, J. K., Briner, J. P., Badgley, J. A., Balter-Kennedy, A.,



927 Graham, B. L., Cluett, A., Lamp, J. L., Schwartz, R., Tuna, T., Bard, E., Caffee, M. W.,
928 Zimmerman, S. R. H., and Schaefer, J. M.: In situ cosmogenic ^{10}Be – ^{14}C – ^{26}Al
929 measurements from recently deglaciated bedrock as a new tool to decipher changes in
930 Greenland Ice Sheet size, *Clim. Past*, 17, 419–450, [https://doi.org/10.5194/cp-17-419-](https://doi.org/10.5194/cp-17-419-2021)
931 2021, 2021.